A Model for the Complex Dielectric Constant of Supercooled Liquid Water at Microwave Frequencies

Philip W. Rosenkranz, *Life Fellow, IEEE*

***Abstract*—Measurements of the complex dielectric constant, or relative permittivity, spectrum of liquid water are modeled for frequencies up to 1 THz and temperatures up to 60 °C by a combination of two components: a Debye function, which characterizes the reorientation of the water molecules under the influence of an electric field, and a distributed-resonance function, which is associated with vibrations of intermolecular hydrogen bonds. This model provides a good representation of cloud measurements below 200 GHz at temperatures as low as −25 °C.**

***Index Terms*—Clouds, microwave propagation, remote sensing, water permittivity.**

I. Introduction

CLOUDS containing supercooled liquid water are distinguishable from ice clouds by a much higher microwave opacity and different frequency dependence. However, recent microwave radiometer measurements of supercooled clouds [1]–[4] have revealed discrepancies between the observed cloud opacities and calculations from published models of liquid water's complex dielectric constant when the cloud temperatures were substantially less than 0 °C. Most of the laboratory measurements from which these models were derived were made at higher temperatures; thus, it is perhaps not surprising that when extrapolated below zero, the models differ among themselves and with the observations.

Microwave radiometry is one of the principal techniques for measurement of cloud liquid water path (LWP) [5]. It would be desirable to bring modeling and observations into better agreement in the supercooled regime because supercooled clouds are fairly common and can exist at temperatures as low as approximately −40 °C [6]. They are an important subject of remote sensing for multiple reasons: They can present a danger of severe icing for aircraft [7]. Clouds of all types are important factors in our understanding of radiation balance in the atmosphere; the U.S. Department of Energy's Atmospheric Radiation Measurement program aims at improved understanding of clouds and their interaction with radiation [8]. In addition, incorrect modeling of liquid water opacity can introduce errors in other parameters retrieved by remote sensing.

Manuscript received April 21, 2014; revised June 12, 2014; accepted July 4, 2014.

P. W. Rosenkranz, retired, was with the Research Laboratory of Electronics, Massachusetts Institute of Technology, Cambridge, MA 02139-4307 USA. He resides in Chestnut Hill, MA USA (e-mail: phil.rosenkranz@alum.mit.edu).

Digital Object Identifier 10.1109/TGRS.2014.2339015

Cloud opacity is the integral of the absorption coefficient along the propagation path. For droplets that are small compared to a wavelength (Rayleigh approximation), the cloud absorption coefficient is given by [9]

$$\alpha(\nu, T, f) = \frac{18\pi\varepsilon'' f\nu}{c\,|\varepsilon + 2|^2} \tag{1}$$

where f is the volume fraction of liquid in the cloud; c is the speed of light; and $\varepsilon = \varepsilon' - i\varepsilon''$ is the complex dielectric constant, or relative permittivity, of liquid water, which is an implicit function of frequency ν and temperature T. Thus, cloud opacity depends on both the real and imaginary parts of ε. The convention by which ε has a negative imaginary part is used here.

In the next section, this paper defines a new model for the frequency dependence of ε. Section III determines the temperature dependence of parameters in the model by adjustment to laboratory measurements of ε and radiometric measurements of cloud opacity ratios. Then, Section IV compares this model with other measurements not used in the fitting, and Section V compares it to some previous models.

II. Complex Dielectric Spectrum of Water

The complex dielectric constant characterizes the collective motion of the molecular dipole moments under the influence of an electric field [10]. In liquid water, the molecules are linked by a disordered network of hydrogen bonds, in which a hydrogen atom of one molecule is attracted to the oxygen atom of another molecule that is located within a distance of a few angstroms. Reorientation of a water molecule requires breaking of a hydrogen bond and reforming it with another molecule. Some insight into this process is provided by the molecular dynamics simulations of Laage and Hynes [11]. In their simulations, switching of a hydrogen bond occurred on a timescale of ∼250 fs. Oscillations about the equilibrium positions of the molecules were seen, but the hydrogen bonds' orientational autocorrelation function decayed exponentially at longer times (> 400 fs). The average number of hydrogen bonds accepted was 1.8 per oxygen atom.

Fig. 1 displays measurements of water's complex dielectric constant in the temperature range of 19.3 °C–20.2 °C from [12]–[20]. At these temperatures, the spectrum is dominated up to ∼100 GHz by the reorientational contribution, indicated by R in the figure. Three bands at higher frequencies can be also

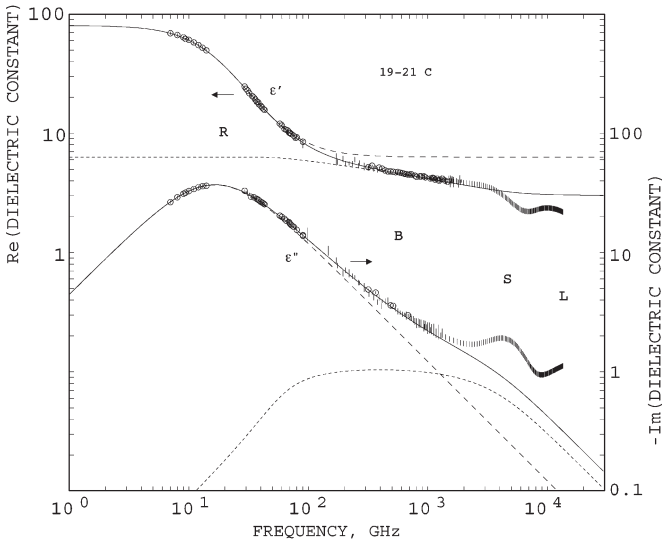

Fig. 1. Real and imaginary parts of water's complex dielectric constant. Measurements are from [12]–[20]. Vertical bars indicate ± 1 standard deviation and are circled when $\leq 3\%$. The long-dashed lines represent the contribution of the R component of the model, plotted as $\varepsilon_s - \Delta_R + \Delta_R F_R(\nu)$; the short-dashed lines are the contribution of the B component, plotted as $\varepsilon_s - \Delta_R - \Delta_B + \Delta_B F_B(\nu)$; and the solid lines are for the combined model $\varepsilon_s - \Delta_R - \Delta_B + \Delta_R F_R(\nu) + \Delta_B F_B(\nu)$.

distinguished in Fig. 1. Walrafen [21], [22] observed these in Raman scattering spectra and identified them (by analogy with the water pentamer) as being due to intermolecular vibrational modes: bending (B) and stretching (S) of hydrogen bonds, both involving translation of molecules, and librational motion (L) of molecules about their centers of mass. If liquid water contains a network of hydrogen bonds, however, it is likely that some mixing of these modes of vibration occurs; bands B and S can be alternatively described as due to hindered translation of the molecules [23]. At higher frequencies than those shown in Fig. 1, other bands associated with intramolecular vibrations are observed [21], [23].

As Ellison [24] has pointed out, there are two equivalent ways to construct a model for the complex dielectric constant

$$\varepsilon(\nu) = \sum_i \Delta_i F_i(\nu) + \varepsilon_\infty \tag{2a}$$

$$= \varepsilon_s - \sum_i \Delta_i \left[1 - F_i\left(\nu\right)\right] \tag{2b}$$

where ε_∞ is the contribution from higher frequency processes that are not included in the model, $\varepsilon_s = \varepsilon(0)$ is the static dielectric constant, and the normalization of the complex shape factors F is such that

$$F_i(0) = 1 \tag{3}$$

$$F_i(\infty) = F_i(-\infty) = 0. \tag{4}$$

The Δ parameters define the amplitude of each band in the model. With these definitions, it follows that:

$$\varepsilon_\infty = \varepsilon_s - \sum_i \Delta_i. \tag{5}$$

This paper is concerned with modeling the frequency range below 1 THz; therefore, only bands R and B will be included. There is fairly general agreement among modelers (e.g., [18] and [24]–[27]) that the reorientational part of the spectrum is well represented by a Debye shape factor

$$F_R(\nu) = \frac{\gamma_R}{\gamma_R + i\nu}. \tag{6}$$

Parameter γ_R multiplied by 2π is the reciprocal of the long-time decay constant of the autocorrelation function for the macroscopic dipole moment.

Most previously published models for water, if they include the contribution of band B at all, have represented it by either one [18], [25]–[27] or two [24] additional Debye shape factors, depending on the frequency range modeled. Although it can be difficult to experimentally distinguish between a nonresonant spectral contribution and a strongly damped resonance, the association of this band with intermolecular vibrations suggests the use of a resonant-band representation. Furthermore, the network of hydrogen bonds in liquid water introduces strong coupling of the vibrations of individual molecular pairs, which can spread their resonant frequencies apart. The molecular environment, particularly the number of hydrogen bonds, also varies on a microscopic scale. These considerations could account for the observed broad width of the bending band, which motivates use of a distributed-resonance representation for it

$$F_B(\nu) = \frac{\log\left[\frac{(z_2 - i\nu)}{(z_1 - i\nu)}\right]}{2\log\left(\frac{z_2}{z_1}\right)} + \frac{\log\left[\frac{\left(z_2^* - i\nu\right)}{\left(z_1^* - i\nu\right)}\right]}{2\log\left(\frac{z_2^*}{z_1^*}\right)} \tag{7}$$

where z_1 and z_2 are complex numbers with negative real parts and positive imaginary parts; an asterisk denotes the complex conjugate. In (7), $\log[]$ is to be understood as the principal value of the complex logarithm, with the angle of its complex argument defined between $-\pi$ and $+\pi$. The properties of (7) are further discussed in the Appendix. The long- and short-dashed lines in Fig. 1 show the contributions of the two components of the model, and the solid lines show the combined model. The curves are calculated for $T = 20\ ^\circ$C using the parameters given in the next section.

III. Temperature Dependence of Parameters in the Model

The static dielectric constant model of Pátek *et al.* [28] is used here

$$\varepsilon_s = -43.7527\theta^{0.05} + 299.504\theta^{1.47} - 399.364\theta^{2.11} + 221.327\theta^{2.31} \tag{8}$$

where $\theta = 300/(T + 273.15)$ for T in Celsius. They fitted their model to the low-frequency measurements of Hamelin *et al.* [29] and Bertolini *et al.* [30] over the temperature range $-16\ ^\circ$C–$110\ ^\circ$C.

For the two R-band parameters, the temperature functions follow the forms recommended by Ellison [24], except that his time constant is converted to a frequency:

$$\Delta_R = 80.69715\exp(-T/226.45) \tag{9}$$

$$\gamma_R = 1164.023\exp\left[-651.4728/(T + 133.07)\right]\ (\text{GHz}). \tag{10}$$

He fitted the above coefficients to a large set of laboratory measurements over the ranges of 0–50 GHz and 0 °C–100 °C. (When Ellison extended his model to higher frequencies, the coefficients for band R were slightly modified, but those values are not used here because of the different formulation for band B.)

The B-band parameters Δ_B, z_1, and z_2 were determined here by fitting the model to the laboratory measurements in [12]–[20] and the cloud measurements in [2] and [4]. In the latter two references, incremental cloud opacities were measured radiometrically. Taking the ratio of opacities at two frequencies for each cloud eliminated the need for an ancillary measurement of LWP, but an estimate of temperature in the cloud was required. The mean radiating temperature of a cloud was assumed in [2] to be the mean of the base and top temperatures, which were obtained from ground-based and satellite infrared radiometers, respectively. This assumption could be a source of error but is unlikely to be a major source, considering that the median absolute difference between the base and top temperatures was 6°. The uncertainty of the mean cloud temperature was estimated to be 2.5° on average. In [4], cloud radar and, for some of the observations, lidar were available to locate the vertical position of the liquid water more precisely.

In the fitting procedure, Ellison's model [24] was used to calculate the contributions from the lower wings of bands S and L, which partially overlap the high-frequency wing of band B. The B-band parameters' values were optimized using the Levenberg–Marquardt method [31] within $\pm 2°$ windows around each of the temperatures $T = -2$ °C, 6 °C, 15 °C, 19 °C, 30 °C, 42 °C, 51 °C, and 58 °C measured in [19] (because that data contributes most to characterizing the shape of band B); to those temperatures, binned averages at 4.1° increments between -25 °C and -4 °C were added from cloud opacity-ratio measurements at 21.4/31.5, 52.3/31.4, 90/31.4, 150/31.4, and 225/31.4 GHz [2], [4]. Then the functions of temperature plotted in Figs. 2 and 3 were fitted to the optimized parameter values.

The model function for band B's amplitude is

$$\Delta_B = 4.008724 \, \exp(-T/103.05). \tag{11}$$

The measurements were not of sufficient precision to determine the temperature dependence of the real and imaginary parts of z_1 independently, but at 19 °C, the optimum value of $-\Re(z_1)$ was found to be 3/4 of $\mathrm{Im}(z_1)$; hence, the model function is

$$z_1 = (-0.75 + i)\nu_1 \tag{12}$$

where

$$\nu_1 = 10.46012 + 0.1454962\, T + 0.063267156 T^2 + 0.00093786645\, T^3 \ (\mathrm{GHz}). \tag{13}$$

Little dependence of z_2 on temperature was found; hence, in the interest of avoiding undue complexity in the model, it is set to a constant value

$$z_2 = -4500 + i\, 2000 \ (\mathrm{GHz}). \tag{14}$$

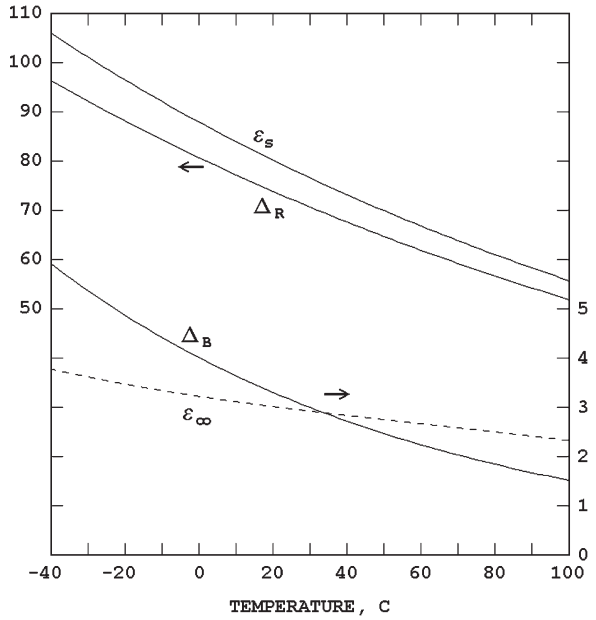

Fig. 2. Temperature dependence of parameters ε_s, Δ_R, Δ_B, and ε_∞.

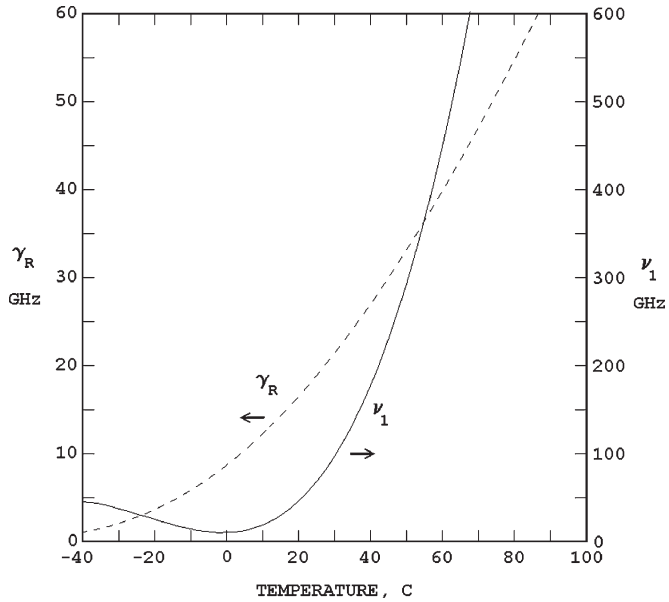

Fig. 3. Temperature dependence of parameters γ_R and ν_1.

The real parts of z_1 and z_2 should not be interpreted as reciprocals of time constants because they have been adjusted to reproduce the shape of a band, rather than an individual resonance.

The solid curve in Fig. 1 provides a comparison of the calculated ε to laboratory measurements near 20 °C, and Fig. 4 shows the fit to opacity-ratio measurements for subzero temperatures. These figures show that the model has sufficient flexibility to adapt to the measurements, given appropriate values for the parameters.

In Fig. 4, each data point for 21.4/31.5 GHz represents an individual cloud. The open circles were corrected for correlated water-vapor variations by means of a third radiometer at 22.235 GHz, i.e., the center frequency of a water-vapor line. The open squares indicate data obtained prior to the installation of that third radiometer channel and therefore without the vapor

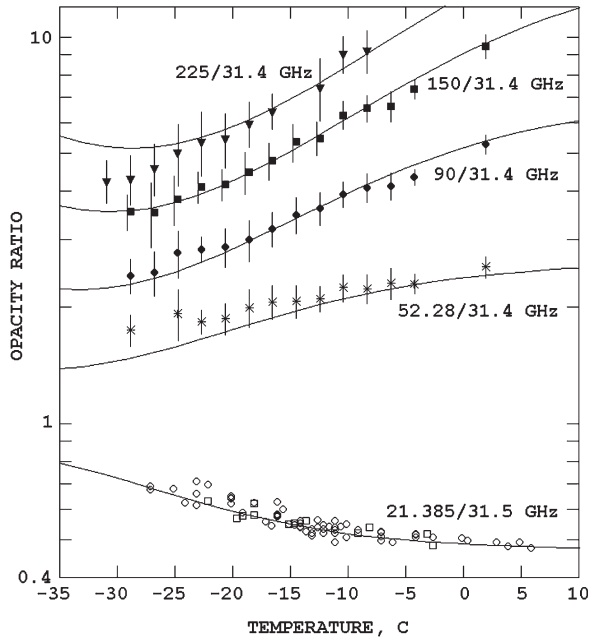

Fig. 4. Cloud absorption ratios measured in [2] at 21.385/31.5 GHz and in [4] at other frequencies. The curves are calculated from equations in the text.

correction. The correction for water-vapor variation is small, as one can judge from the overlap of the two groups of data. At the other frequencies, each symbol represents a temperature-binned average of opacity ratios with ± 1 standard-deviation error bars, as in [4].

IV. Comparisons With Other Measurements

The most challenging range of temperature for a modeling effort is below zero. The accuracy of the model below -2 °C depends largely on the extrapolation of (9) and (10) to subzero temperatures at 31 GHz because opacity ratios do not provide information on the magnitude of the cloud opacity. This section compares model calculations to some measurements that were not used in the fitting of the coefficients.

Cadeddu and Turner [1] measured cloud opacities with 23.8-, 31.4-, 90-, 150-, and 170-GHz radiometers. The cloud temperature was measured by radiosondes, and an infrared interferometer provided an estimate of LWP through the cloud. The use of infrared measurements for LWP limited this technique to relatively thin clouds and also may have contributed some systematic error because of uncertainty about temperature dependence of the infrared refractive index, as discussed in [1]. Fig. 5 shows their measurements of cloud absorption, averaged in 10° temperature bins and plotted at the central temperature of each bin, along with calculations from the present model. The 1σ error brackets shown in Fig. 5 include estimates of systematic errors, which, with respect to LWP error, would act in the same proportion at all five frequencies. Although the two highest frequencies in Fig. 5 exhibit stronger temperature dependence than implied by the ratios in Fig. 4, their error brackets nearly overlap the calculated values.

Dielectric constant measurements that extend substantially below 0 °C have been done in the laboratory by Bertolini *et al.* [30] at 9.61 GHz and by Risman and Wäppling-

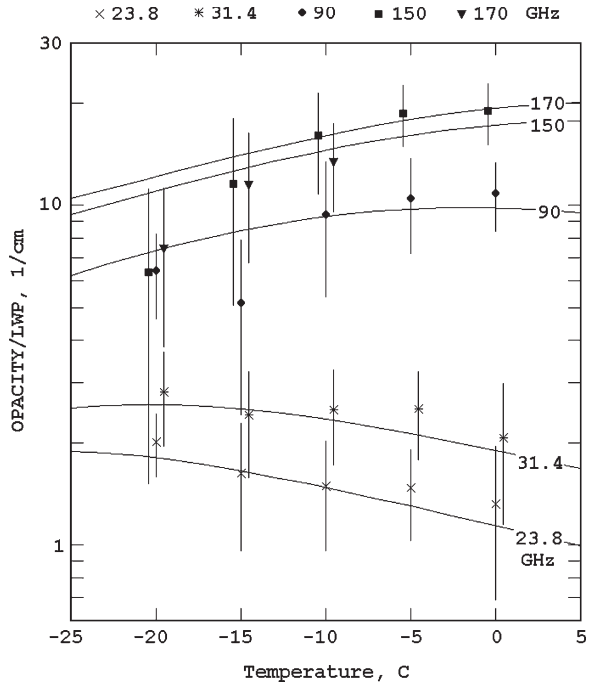

Fig. 5. Cloud absorption measured in [1]. Data points at 31.4, 150, and 170 GHz are slightly shifted in temperature for legibility. The curves are calculated from equations in the text.

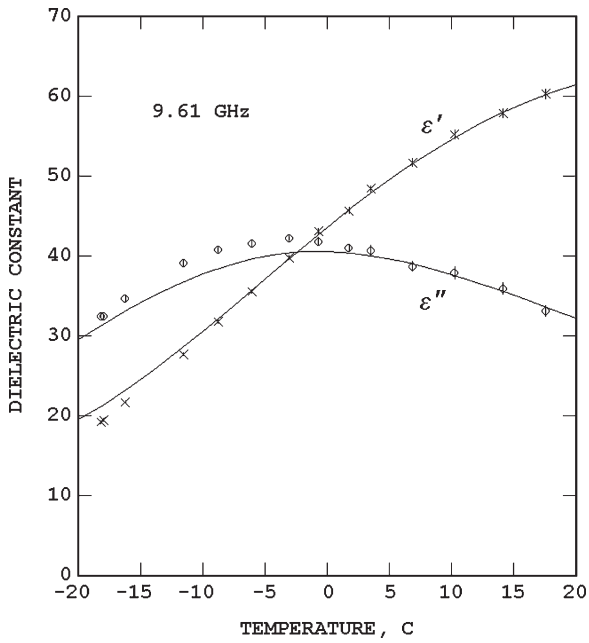

Fig. 6. Complex dielectric constant at 9.61 GHz, measured in [30]. The curves are calculated from equations in the text.

Raaholt [32] at 920 MHz. In both cases, the water was confined in narrow glass tubes to inhibit freezing. Figs. 6 and 7 display those measurements. The value of γ_R passes through 9.61 GHz within the temperature range plotted in Fig. 6, which causes the peak in the imaginary part of ε and the monotonic increase with temperature in the real part. The much lower measurement frequency in Fig. 7, on the other hand, is on the lower wing of band R, which accounts for the decrease in both parts of ε as γ_R increases with temperature and ε_s decreases. The vertical bars through the data points in Figs. 6 and 7 reflect the uncertainties

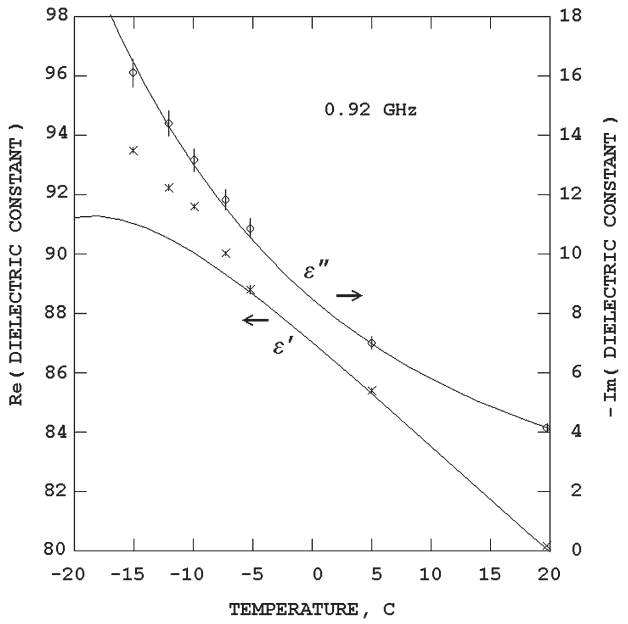

Fig. 7. Complex dielectric constant at 0.92 GHz, measured in [32]. The curves are calculated from equations in the text.

TABLE I
RMS DIFFERENCES BETWEEN MODELS AND MEASUREMENTS IN [12]–[20], $0 \leq T \leq 37$ °C AND $\nu < 500$ GHz

	this paper	ref. [18]	ref. [24]
Re(ε)	2.4%	3.6%	4.2%
Im(ε)	4.2%	5.1%	5.0%

assigned to the measurements by their respective authors. In the case of Fig. 6, it is not clear from the reference whether systematic uncertainties were included in the error estimates.

The model provides a satisfactory fit to ε' in Fig. 6 and ε'' in Fig. 7. The discrepancies in Fig. 7 in ε' are related to the inconsistency noted by Risman and Wäppling-Raaholt [32] between the extrapolation of their measurements to ε_s and the 27.5-MHz measurements in [30], to which (8) was fitted at subzero temperatures. For example, at -15 °C Risman and Wäppling-Raaholt obtained 96.4 for the static dielectric constant, as compared with 94.3 from (8).

V. COMPARISONS WITH OTHER MODELS

To place these results in the context of previous modeling work, Tables I and II compare the RMS differences between measurements and model predictions for the present model and two others: the freshwater model of Stogryn *et al.* [18], which had been considered the best fit of previously published models to the cloud measurements, and the model of Ellison [24], the most up-to-date of the models derived from laboratory measurements. References [1] and [2] show similar comparisons for several other models.

Table I compares percentage, i.e., 100 × (model-measurement)/measurement, RMS differences for the measurements in [12]–[20] at frequencies < 500 GHz, and temperatures 0 °C–37 °C, which are the ranges of applicability stated in [18]. The intended ranges of [24] are 0–25 THz and 0 °C–100 °C. Typical measurement uncertainty is ∼3%, and measurements with relative uncertainties >15% were excluded from the comparisons. All three models fit the measurements reasonably well, which is undoubtedly attributable to the fact that these measurements, or most of them, were used in deriving each model. However, model differences may be detectable in some applications; for example, at frequencies above ∼30 GHz, the calculated brightness temperature of a freshwater surface can differ among the models by amounts exceeding 1 K.

In the first row of Table II, i.e., RMS opacity percentage differences for the data of [1], the model temperature is set to the center of the measurement range. At subzero temperatures, the models of [18] and [24] are being extrapolated outside their intended range. The improvement obtained in the first row with the present model occurs at the higher frequencies and lower temperatures and is attributable to the different treatment of band B. In particular, the upturn of ν_1 for $T < 0$, which is shown in Fig. 3, seems necessary to fit the cloud measurements. Increasing ν_1 implies that the lower wing of band B recedes toward higher frequencies as T decreases below zero. This effect is illustrated in Fig. 8, where the -20 °C data in Fig. 5 is replotted along with curves calculated from the three models. The models [18] and [24] represent the lower extent of band B by a second Debye function; in [18], the second relaxation frequency has a constant value of 159 GHz, whereas in [24], it monotonically decreases with decreasing temperature, reaching the value of 7.24 GHz at -20 °C.

In the last two rows of Table II, ε' and ε'' were combined in calculating the RMS, and only measurements at $T < 0$ °C were included. Ellison's model is a better fit at 9.6 GHz, but the model of Stogryn *et al.* has more difficulty reproducing the laboratory measurements at subzero temperatures.

VI. CONCLUSIONS AND SUGGESTIONS FOR FUTURE WORK

Overall, calculations of the opacity of supercooled clouds with the new model are more accurate, particularly at the higher microwave frequencies. However, laboratory measurements of supercooled water at frequencies in the 20–200-GHz range would be very useful for validation. If desired for an application, the present model could be extended to frequencies above 1 THz by adding the contributions of the S and L bands from Ellison's model [24] (where they are denoted as resonances), but complex-conjugated because of the different sign convention for Im(ε). However, until measurements at temperatures substantially below zero are available, there appears to be little opportunity for improvement on his model at those frequencies.

This paper has treated the case of pure water, but (7) may also find use in modeling saline water. However, aside from the added conductivity, the dielectric parameter values can differ from those of freshwater due to the dissolved salt.

APPENDIX
DISCUSSION OF EQUATION (7)

If in (7) one replaces $i\nu$ by the complex frequency $z = \eta + i\nu$, then the singularities of $F_B(z)$ in the z-plane consist

TABLE II
RMS DIFFERENCES BETWEEN MODELS AND MEASUREMENTS AT SUBZERO TEMPERATURES

measurement type	this paper	ref. [18]	ref. [24]
Cloud absorption at 23.8 to 170 GHz [1]	27%	48%	39%
Complex dielectric constant at 9.61 GHz [30]	2.1	3.6	1.5
Complex dielectric constant at 918 Mhz [32]	1.6	2.2	1.6

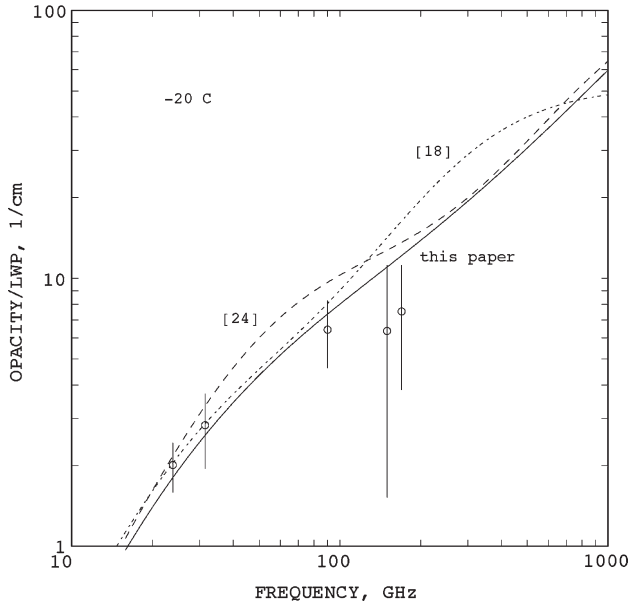

Fig. 8. Cloud absorption at −20 °C measured in [1] and calculated from three models.

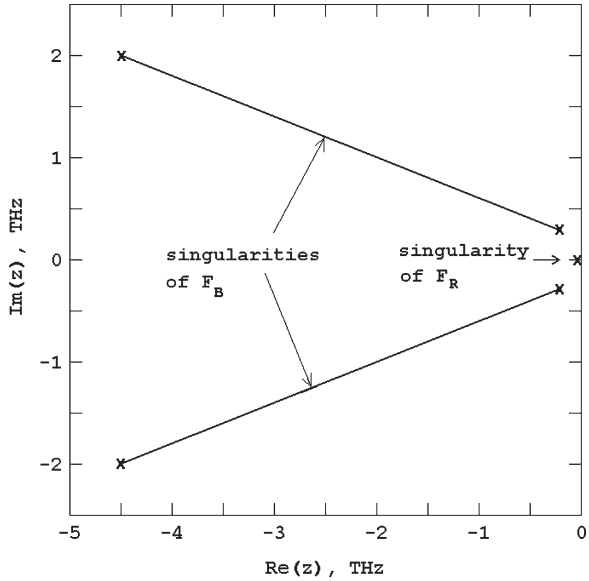

Fig. 9. Singularities of the functions $F_R(z)$ and $F_B(z)$ in the complex frequency plane at 50 °C.

of branch points at z_1 and z_2 with a branch cut extending between those points, and conjugately located singularities extending from z_1^* to z_2^*, as depicted in Fig. 9. In contrast, $F_R(z)$ has a single first-order pole at $z = -\gamma_R$. Both functions are analytic where $\eta > 0$. That, and the fact that they are finite on the entire ν-axis, are necessary and sufficient conditions for the real and imaginary parts of these shape factors to satisfy the Kramers–Kronig relations [10]. Equation (7) also satisfies the following relation:

$$F_B(-\nu) = F_B^*(\nu) \tag{A1}$$

which is necessary if the spectrum corresponds to a real impulse response.

The numerator of the first term on the right side of (7) can be derived by an integration in which the location of a first-order pole moves along the line extending from z_1 to z_2 in the complex plane

$$\log \frac{z_2 - i\nu}{z_1 - i\nu} = \int_{z_1}^{z_2} \frac{dz'}{z' - i\nu} \tag{A2}$$

and likewise, the second term's numerator is the result of an integration from z_1^* to z_2^*. Then the normalization condition (3) leads to (7). Hence, $F_B(\nu)$ corresponds to resonances distributed over a band, which allows it to fit the broad B-band closely.

In the special case that z_1 and z_2 are both real, $F_B(\nu)$ is equivalent to the shape factor derived by Fröhlich [33], and independently in [34] and [35], for a distribution of relaxation time constants. Another special case is the limit $z_2 \to z_1$, where application of l'Hôpital's rule to (7) shows that it approaches a Van Vleck–Weisskopf [36] shape factor.

The complex logarithm can be expressed in terms of the real and imaginary parts of its argument as

$$\log(x + iy) = \frac{1}{2}\log\left(x^2 + y^2\right) + i\tan^{-1}(y, x) \tag{A3}$$

where the inverse tangent takes values from $-\pi$ to $+\pi$.

ACKNOWLEDGMENT

The author would like to thank C. Mätzler for helpful discussions and for comments on the manuscript and S. Kneifel for providing numerical values of his data.

REFERENCES

[1] M. P. Cadeddu and D. D. Turner, "Evaluation of water permittivity models from ground-based observations of cold clouds at frequencies between 23 and 170 GHz," *IEEE Trans. Geosci. Remote Sens.*, vol. 49, no. 8, pp. 2999–3008, Aug. 2011.

[2] C. Mätzler, P. W. Rosenkranz, and J. Cermak, "Microwave absorption of supercooled clouds and implications for the dielectric properties of water," *J. Geophys. Res.*, vol. 115, no. D23, pp. D23208-1–D23208-12, Dec. 2010.

[3] C. Mätzler and J. Morland, "Refined physical retrieval of integrated water vapor and cloud liquid for microwave radiometer data," *IEEE Trans. Geosci. Remote Sens.*, vol. 47, no. 6, pp. 1585–1594, Jun. 2009.
[4] S. Kneifel *et al.*, "Absorption properties of supercooled liquid water between 31 and 225 GHz: Evaluation of absorption models using ground-based observations," *J. Appl. Meteor. Climatol.*, vol. 53, no. 4, pp. 1028–1045, Apr. 2014.
[5] D. D. Turner *et al.*, "Retrieving liquid water path and precipitable water vapor from the atmospheric radiation measurement (ARM) microwave radiometers," *IEEE Trans. Geosci. Remote Sens.*, vol. 45, no. 11, pp. 3680–3690, Nov. 2007.
[6] Y. Hu *et al.*, "Occurrence, liquid water content, fraction of super cooled water clouds from combined CALIOP/IIR/MODIS measurements," *J. Geophys. Res.*, vol. 115, no. D4, pp. D00H34-1–D00H34-13, Feb. 2010.
[7] M. K. Politovich, "Aircraft icing caused by large super cooled droplets," *J. Appl. Meteor.*, vol. 28, no. 9, pp. 856–868, Sep. 1989.
[8] C. Zhao *et al.*, "Toward understanding of differences in current cloud retrievals of ARM ground-based measurements," *J. Geophys. Res.*, vol. 117, no. D10, pp. D10206-1–D10206-21, May 2012.
[9] C. Mätzler and M. Schwank, "Dielectric properties of heterogeneous media," in *Thermal microwave radiation: Applications for remote sensing*, C. Mätzler, Ed. London, U.K.: IET, 2006, sec. 5.7.
[10] C. J. F. Böttcher and P. Bordewijk, *Theory of Electric Polarization, Vol. 2: Dielectrics in Time-Dependent Fields*. Amsterdam, The Netherlands: Elsevier, 1978.
[11] D. Laage and J. T. Hynes, "A molecular jump mechanism of water reorientation," *Science*, vol. 311, no. 5782, pp. 832–835, Feb. 2006.
[12] J. B. Hasted, S. K. Husain, F. A. M. Frescura, and J. R. Birch, "The temperature variation of the near millimetre wavelength optical constants of water," *Infrared Phys.*, vol. 27, no. 1, pp. 11–15, Jan. 1987.
[13] J. M. Alison and R. J. Sheppard, "A precision waveguide system for the measurement of complex permittivity of lossy liquids and solid tissues in the frequency range 29 GHz to 90 GHz—I," *Meas. Sci. Tech.*, vol. 1, no. 10, pp. 1093–1098, Oct. 1990.
[14] M. G. M. Richards and R. J. Sheppard, "A precision waveguide system for the measurement of complex permittivity of lossy liquids and solid tisssues in the frequency range 29 GHz to 90 GHz—II," *Meas. Sci. Tech.*, vol. 2, no. 7, pp. 663–667, Jul. 1991.
[15] J. M. Alison and R. J. Sheppard, "A precision waveguide system for the measurement of complex permittivity of lossy liquids and solid tisssues in the frequency range 29 GHz to 90 GHz—III," *Meas. Sci. Tech.*, vol. 2, no. 10, pp. 975–979, Oct. 1991.
[16] X. Hu, H. A Buckmaster, and O. Barajas, "The 9.355 GHz complex permittivity of light and heavy water from 1 to 90 °C," *J. Chem. Eng. Data*, vol. 39, no. 4, pp. 625–638, Oct. 1994.
[17] H. R Zelsmann, "Temperature dependence of the optical constants for liquid H_2O and D_2O in the far IR region," *J. Molecular Struct.*, vol. 350, no. 2, pp. 95–114, May 1995.
[18] A. P. Stogryn, H. T. Bull, K. Rubayi, and S. Iravanchy, "The Microwave Permittivity of Sea and Fresh Water," Aerojet, Sacramento, CA, USA, Aerojet internal report, 1995.
[19] C. Rønne *et al.*, "Investigation of the temperature dependence of dielectric relaxation in liquid water by THz reflection spectroscopy and molecular dynamics simulation," *J. Chem. Phys.*, vol. 107, no. 14, pp. 5319–5331, 1997.
[20] K. Lamkaouchi, A. Balana, G. Delbos, and W. J. Ellison, "Permittivity measurements of lossy liquids in the range 26–110 Ghz," *Meas. Sci Tech.*, vol. 14, no. 4, pp. 444–450, Apr. 2003.
[21] G. E. Walrafen, "Raman spectral studies of water structure," *J. Chem. Phys.*, vol. 40, no. 11, pp. 3249–3256, 1964.
[22] G. E. Walrafen, "Raman spectral studies of the effects of temperature on water and electrolyte solutions," *J. Chem. Phys.*, vol. 44, no. 4, pp. 1546–1558, Feb. 1966.
[23] D. Eisenberg and W. Kauzmann, *The Structure and Properties of Water*. Oxford, U.K.: Oxford Univ. Press, 1969.
[24] W. Ellison, "Permittivity of pure water, at standard atmospheric pressure, over the frequency range 0–25 THz and the temperature range 0–100 C," *J. Phys. Chem. Ref. Data*, vol. 36, no. 1, pp. 1–17, Mar. 2007.
[25] W. Ellison, "Freshwater and sea water," in *Thermal Microwave Radiation: Applications for Remote Sensing*, C. Mätzler, Ed. London, U.K.: IET, 2006, sec. 5.2.
[26] H. J. Liebe, G. A. Hufford, and T. Manabe, "A model for the complex permittivity of water at frequencies below 1 THz," *Int. J. Infrared Millim. Waves*, vol. 12, no. 7, pp. 659–675, Jul. 1991.
[27] T. Meissner and F. J. Wentz, "The complex dielectric constant of pure and sea water from microwave satellite observations," *IEEE Trans. Geosci. Remote Sens.*, vol. 42, no. 9, pp. 1836–1849, Sep. 2004.
[28] J. Pátek, J. Hrubý, J. Klomfar, and M. Soucková, "Reference correlations for thermodynamic properties of liquid water at 0.1 MPa," *J. Phys. Chem. Ref. Data*, vol. 38, no. 1, pp. 21–29, 2009.
[29] J. Hamelin, J. B. Mehl, and M. R. Moldover, "The static dielectric constant of liquid water between 274 and 418 K near the saturated vapor pressure," *Int. J. Thermophys.*, vol. 19, no. 5, pp. 1359–1380, Sep. 1998.
[30] D. Bertolini, M. Cassettari, and G. Salvetti, "The dielectric relaxation time of supercooled water," *J. Chem. Phys.*, vol. 76, no. 6, pp. 3285–3290, Mar. 1982.
[31] W. H. Press, S. A. Teukolsky, W. T. Vetterling, and B. P. Flannery, *Numerical Recipes in Fortran: The Art of Scientific Computing*, 2nd ed. Cambridge, U.K.: Cambridge Univ. Press, 1992.
[32] P. O. Risman and B. Wäppling-Raaholt, "Retro-modelling of a dual resonant applicator and accurate dielectric properties of water from -20 °C to $+100$ °C," *Meas. Sci. Tech.*, vol. 18, no. 4, pp. 959–966, Apr. 2007.
[33] H. Fröhlich, *Theory of Dielectrics*. Oxford, U.K.: Clarendon, 1958.
[34] C. Svensson and G. E. Dermer, "Time domain modeling of lossy interconnects," *IEEE Trans. Adv. Packag.*, vol. 24, no. 2, pp. 191–196, 2001.
[35] A. R. Djordjevic, R. M. Biljic, V. D. Likar-Smiljanic, and T. K. Sarkar, "Wideband frequency-domain characterization of FR-4 and time-domain causality," *IEEE Trans. Electromagn. Compat.*, vol. 43, no. 4, pp. 662–667, Nov. 2001.
[36] J. H. Van Vleck and V. F. Weisskopf, "On the shape of collision-broadened lines," *Rev. Mod. Phys.*, vol. 17, no. 2/3, pp. 227–236, Apr. 1945.

Philip W. Rosenkranz (S'68–M'71–SM'84–F'97–LF'11) received the S.B., S.M., and Ph.D. degrees from the Massachusetts Institute of Technology (MIT), Cambridge, MA, USA, in 1967, 1968, and 1971, respectively, all in electrical engineering.

He did postdoctoral work in the Jet Propulsion Laboratory, California Institute of Technology, Pasadena, CA, USA. In 1973, he joined the Research Staff of the Research Laboratory of Electronics, MIT, where from 1989 until retirement in 2007, he was a Principal Research Scientist. His field of interest is the interaction of electromagnetic waves with constituents of the terrestrial atmosphere and surface, and remote sensing of geophysical parameters from aircraft and satellites. Examples of this work are theoretical models for absorption by molecular oxygen and water vapor, and measurement of temperature, water vapor, and cloud liquid water with microwave radiometers.